Effects of upstream boundary layer on the unsteadiness of shock-induced separation

B. GANAPATHISUBRAMANI†,
N. T. CLEMENS AND D. S. DOLLING

Center for Aeromechanics Research, The University of Texas at Austin, Austin, TX 78712, USA

The relationship between the upstream boundary layer and the low-frequency, large-scale unsteadiness of the separated flow in a Mach 2 compression ramp interaction is investigated by performing wide-field particle image velocimetry (PIV) and planar laser scattering (PLS) measurements in streamwise–spanwise planes. Planar laser scattering measurements in the upstream boundary layer indicate the presence of spanwise strips of elongated regions of uniform momentum with lengths greater than 40δ. These long coherent structures have been observed in a Mach 2 supersonic boundary layer (Ganapathisubramani, Clemens & Dolling 2006) and they exhibit strong similarities to those that have been found in incompressible boundary layers (Tomkins & Adrian 2003; Ganapathisubramani, Longmire & Marusic 2003). At a wall-normal location of $y/\delta = 0.2$, the inferred instantaneous separation line of the separation region is found to oscillate between $x/\delta = -3$ and -1 (where $x/\delta = 0$ is the ramp corner). The instantaneous spanwise separation line is found to respond to the elongated regions of uniform momentum. It is shown that high- and low-momentum regions are correlated with smaller and larger size of the separation region, respectively. Furthermore, the instantaneous separation line exhibits large-scale undulations that conform to the low- and high-speed regions in the upstream boundary layer. The low-frequency unsteadiness of the separation region/shock foot observed in numerous previous studies can be explained by a turbulent mechanism that includes these elongated regions of uniform momentum.

1. Introduction

Shock wave/boundary layer interactions remain an active research topic owing to the problems they present to the design of supersonic aircraft, missiles and projectiles. Sufficiently strong interactions cause severely turbulent and highly unsteady separation of the boundary layer (Andreopoulos, Agui & Briassulis 2000; Dolling 2001; Smits & Dussauge 1996). The presence of turbulent separation can result in large fluctuating pressure loads and high heat transfer rates, and can cause damage or rapid fatigue of aero-structures.

It is well documented that shock-induced turbulent separation is characterized by unsteady motions that exhibit a wide range of frequencies and length scales (results are compiled in a review article by Dolling 1993). The unsteady motions of the interaction include small-scale fluctuations, related to boundary layer and shear layer

† Present address: Department of Aeronautics, Imperial College London, Prince Consort Road, London SW7 2AZ, UK.

turbulence, as well as large-scale, low-frequency pulsations of the separation bubble. Many previous studies of interaction unsteadiness have focused on the dynamics of the separation shock, or specifically the separation *shock foot* (defined as the point where the separation shock meets the wall), because the shock foot can be readily located by using fast-response wall-mounted pressure transducers. In a review of the literature, Dolling (1998) argues that the low-frequency motions are the most important to understand because they have posed the biggest challenge to theoretical and computational models. Typically, the lowest frequency of motion of the shock foot is at least an order of magnitude lower than the nominal boundary layer frequency based on boundary layer thickness (δ). Explaining the cause of this low-frequency motion of the shock foot continues to be a consuming aspect of research into shock-induced separation, owing to the difficulty in associating such low frequencies with typical turbulent mechanisms.

Plotkin (1975) proposed a mathematical model based on convective displacement and a linear restoring mechanism to explain the low-frequency unsteadiness of the shock foot. Plotkin (1975) claimed that the shock foot is convected upstream or downstream from its mean location with the passage of each turbulent eddy (i.e. convected by the velocity fluctuations in the boundary layer), while the stability of the mean flow tends to restore the shock foot to its original position. He assumed that the restoring mechanism was linear and concluded that the shock foot motion is mathematically analogous to the velocity of a particle undergoing Brownian motion. Although Plotkin's work provides a plausible mathematical model, it does not provide a clear physical model that might be responsible for the low-frequency unsteadiness.

There is growing evidence in the literature that the large-scale unsteadiness of shock-induced turbulent separation is driven by the velocity fluctuations in the upstream boundary layer. Andreopoulos & Muck (1987) studied Mach 3 compression ramp interactions with fluctuating pressure transducers and concluded that the shock motion is driven by turbulence in the incoming boundary layer. Their measurements of the shock zero-crossing frequency (defined as the number of back-and-forth crossings of the shock foot across a single transducer) were of the same order of magnitude as the bursting frequency of the incoming turbulent boundary layer. One problem with the Andreopolis & Muck conclusions, however, is that it was shown, later, that their method for detecting the shock foot location tended to overestimate the frequencies of shock motion (Dolling & Brusniak 1989). Erengil & Dolling (1993) made fast-response pressure measurements in a Mach 5 compression ramp interaction and argued that the shock foot unsteadiness reflects a superposition of high- and low-frequency motions. They argue that the high-frequency 'jitter' is caused by the response of the separation shock to the passage of individual turbulent structures, whereas the low-frequency motions of the separation shock are in fact driven by large-scale pulsations of the separation bubble; however, they were not able to identify the cause of the large-scale pulsations of the separation bubble.

McClure (1992) investigated correlations between fluctuations in the upstream boundary layer and motion of the shock foot in Mach 5 compression ramp interactions. He used fluctuating-Pitot probes in the upstream boundary layer and fast-response static pressure transducers under the intermittent region to monitor the instantaneous shock foot position. (The intermittent region is defined as the region of separation shock foot motion.) It was found by conditional averaging that downstream (upstream) sweeps of the shock foot tended to be correlated with rising (falling) Pitot pressure. He concluded that the correlation was better as the Pitot probe was moved closer to the wall and the length scale of rising/falling Pitot pressure was of order

20–40δ. Ünalmis & Dolling (1994) re-examined McClure's data and looked for correlations between the upstream Pitot pressure and shock foot location rather than motion. They found that high Pitot pressure in the upstream boundary layer tended to be correlated with the shock foot being located downstream of its mean position. Similarly, low Pitot pressure in the upstream boundary layer was correlated with an upstream location of the shock foot. They argued that this result is consistent with a model where the shock foot is driven by a low-frequency thickening and thinning of the upstream boundary layer. Furthermore, based on cross-correlations of spanwise-spaced Pitot probes, Ünalmis & Dolling (1998) proposed that stationary streamwise structures are embedded in the boundary layer and that they may be the cause of the low-frequency motion.

This proposed mechanism was tested by Beresh, Clemens & Dolling (2002) in a Mach 5 compression ramp interaction by using particle image velocimetry (PIV) in the upstream boundary layer together with fluctuating pressure measurements to monitor the location of the shock foot. They found a systematic correlation between streamwise velocity fluctuations in the upstream boundary layer and motion of the shock foot. It was found that the shock foot has a tendency to move downstream when the velocity fluctuations in the upstream boundary layer are positive (i.e. the velocity profile is fuller than the mean) and conversely the shock foot moves upstream if the velocity fluctuations in the boundary layer are negative. Beresh *et al.* (2002) did not, however, find a correlation with boundary layer thickness, in seeming contradiction to the studies of Ünalmis & Dolling. Hou, Clemens & Dolling (2003) also made combined PIV and fluctuating pressure measurements, but in a Mach 2 compression ramp interaction. In agreement with Beresh *et al.* (2002), they found that the shock foot motion is correlated with velocity fluctuations in the lower part of the upstream boundary layer. However, unlike the results from Beresh *et al.* (2002), Hou *et al.* (2003) also showed that there is a clear correlation between thickening and thinning of the upstream boundary layer and the shock foot motion. These are not necessarily independent correlations, however, since a thicker boundary layer is associated with a lower velocity near the wall and vice versa. It was found that the shock foot moves upstream (downstream) if the upstream boundary layer is locally thick (thin).

To date it has been difficult to reconcile the low-frequency motion of the shock foot/separation region with any particular turbulent mechanism, since typical turbulent structures are believed to be of scale δ. In most studies (referenced in this section), the boundary layer frequency based on the free-stream velocity (U_∞) and δ is in the range 30–50 kHz. However, Brusniak & Dolling (1994) reported that the dominant shock motion frequency is between 0.4 kHz and 2 kHz. There is an order of magnitude difference between the boundary layer frequency and the frequency of the observed shock motion. Therefore, it would require structures with scales that are an order of magnitude larger than δ to account for the low frequencies that are observed.

Studies in incompressible turbulent boundary layers by various researchers using PIV have shown the existence of long coherent regions of streamwise velocity fluctuations in the log region which extend to lengths of greater than 2δ (Tomkins & Adrian 2003, Ganapathisubramani *et al.* 2003). Hutchins, Ganapathisubramani & Marusic (2004) performed hot-wire measurements and found that these long low- and high-speed regions are as long as 20δ. These elongated structures were also found in a DNS computation of a channel flow performed by del Alamo *et al.* (2004).

The information on the spatial structure of velocity fluctuations in supersonic boundary layers is very limited. The presence of large-scale structures in supersonic boundary layers has been noted in correlation-based studies by Owen & Horstmann

(1972) and Ünalmis & Dolling (1998), where the structures remained coherent sufficiently long to convect several boundary layer thicknesses downstream. However, similar correlation-based studies by Smits *et al.* (1989) found that the large-scale motions in supersonic flows do not extend as far downstream as they do in incompressible flows. Samimy, Arnette & Elliot (1994) performed instantaneous flow visualization measurements and found elongated longitudinal streamwise structures in the outer layer of the boundary layer. Conversely, similar visualization studies by Smith & Smits (1995) do not obviously reveal the presence of elongated structures. Recently, Ganapathisubramani *et al.* (2006) performed wide-field PIV measurements in streamwise–spanwise planes in the log region of a Mach 2 supersonic boundary layer (the same facility utilized in the present study, without the compression ramp). The authors identified the presence of long low- and high-speed regions that extended to lengths greater than 8δ and speculated that these large-scale structures could be a mechanism that drives the low-frequency unsteadiness of the shock foot/separation region.

   This study can be considered a continuation of the work by Ganapathisubramani *et al.* (2006) as we aim to investigate the relationship between the upstream boundary layer and the unsteadiness of the separated flow in a Mach 2 compression ramp interaction. The primary diagnostics used are wide-field particle image velocimetry (PIV) and high-speed condensed-fog planar laser scattering (PLS) measurements in streamwise–spanwise planes. The objective of the current work is to apply these imaging techniques to investigate the relationship between these long, low-frequency, large-scale uniform momentum regions and the unsteady motion of the shock-induced turbulent separation region.

2. Experimental facility and details

2.1. *Wind tunnel facility*

All of the experiments were conducted in the Mach 2 blowdown tunnel of the University of Texas at Austin. The constant-area test section is 6 in. (15.2 cm) wide by 6.3 in. (16 cm) high and had a length of 30 in. (76.2 cm). Removable side doors allowed access to an instrumented floor section. The sidewalls of the test section are equipped with fused silica windows, which are 6 in. (15.2 cm) long by 2 in. (5.1 cm) high by 0.75 in. (1.9 cm) thick, to facilitate the passage of laser sheets used as a source of illumination in PIV and PLS. The top wall of the tunnel was fitted with an acrylic window for optical access of size 8 in. (20.3 cm) long, 2.5 in. (6.4 cm) wide and 0.75 in. (1.9 cm) thick. A total of about 4 m^3 of compressed air was provided by a Worthington HB4 four-stage compressor and stored in external tanks at a pressure of about 2500 p.s.i.a. The stagnation chamber pressure and temperature for the present experiments were approximately 261 ± 7 kPa and 292 ± 5 K, respectively. For these stagnation conditions, stable run times of up to 40 seconds could be obtained. The free-stream conditions were as follows: Mach number $M_\infty = 2$ and velocity $U_\infty = 510$ m s^{-1}. The incoming turbulent boundary layer underwent natural transition and developed under approximately adiabatic wall temperature conditions. The boundary layer properties were as follows: boundary layer thickness $\delta = 12.5$ mm, momentum thickness $\theta = 0.9$ mm, displacement thickness $\delta^* = 2.6$ mm, skin friction velocity $u_\tau = 18.5$ m s^{-1}, Reynolds number based on momentum thickness, $Re_\theta = U_\infty \theta / \nu_\infty = 35\,000$. The Reynolds number based on the skin friction velocity and boundary layer thickness, $Re_\tau = U_\tau \delta / \nu_w = 5600$ (where ν_w is the kinematic viscosity at the wall).
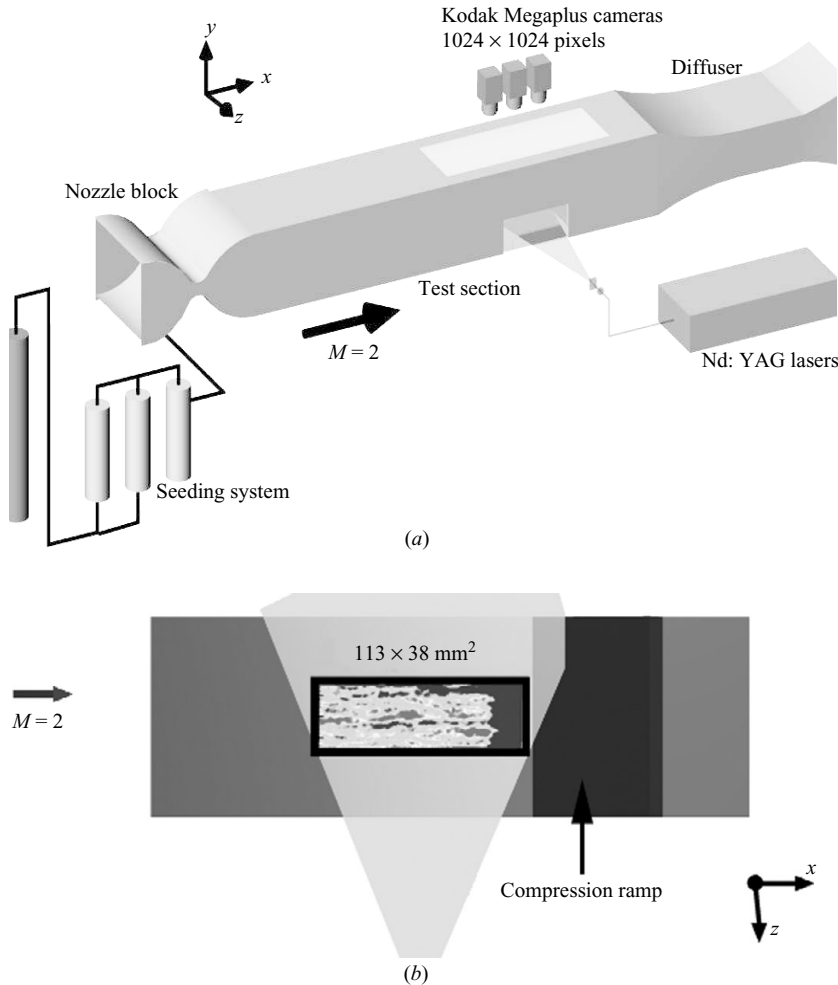
FIGURE 1. Experimental setup: (*a*) perspective view, and (*b*) top view.

Finally, the shock/boundary layer interaction was generated using a 0.9 in. (23 mm) high 20° compression ramp that spanned the width of the test section.

2.2. *Particle image velocimetry* (*PIV*)

The wide-field PIV system used pulsed laser sheets from a dual-cavity flashlamp pumped Nd:YAG laser (Spectra Physics PIV 400) separated in time by 2 μs and directed through one side window and oriented parallel to the tunnel floor as shown in figure 1. The laser pulse energy was 40 mJ, and the thickness of the sheets was about 0.7 mm. Sets of digital images were captured by three Kodak Megaplus CCD cameras (1024×1024 pixels) lined up next to each other in the streamwise direction as shown in figure 1. Nikon MicroNikkor 105 mm f/2.4 lenses were used with all three cameras. The field of view for each camera is approximately 38×38 mm^2 ($\approx 3\delta \times 3\delta$) which results in a magnification of 37 μm/pixel. The total field of view between the three cameras is approximately 113×38 mm^2 ($\approx 9\delta \times 3\delta$). The system was synchronized such that each camera simultaneously imaged the laser sheets. Three pulse-delay generators (Stanford Research Systems DG535) were used to synchronize the PIV system and to

trigger the individual components. Data were acquired at two wall-normal locations, one in the logarithmic region ($y/\delta = 0.2$) and the other in the outer region ($y/\delta = 0.7$). A total of 750 images were acquired at each station, which was adequate for statistical convergence of mean and r.m.s. statistics of the velocity components.

Titanium dioxide (TiO_2) with a manufacturer-specified primary particle diameter of $0.02\,\mu m$ was used as seed particles for PIV. The particles were seeded upstream of the stagnation chamber of the tunnel by using a two-stage fluidized-bed seeder followed by a cyclone separator. The particle seeders were driven by compressed nitrogen. Previous studies have shown that this seeding system produces excellent seeding densities for PIV. Hou (2003) discusses in detail the measurement of the response time of the PIV seed particles used in this study. Time response measurement of the particles through a normal shock indicated that the response time τ_p was about $2.6\,\mu s$. From the response time, the effective (agglomerated) diameter was estimated to be $d_p = 0.26\,\mu m$. Samimy & Lele (1991) suggested that, for particles to faithfully track the velocity fluctuations in a turbulent mixing layer, the Stokes number defined as $St = \tau_p/\tau_f$ (with $\tau_f = \delta/U$, the characteristic flow time scale) must be less than about 0.5. The Stokes number based on the outer time scale of boundary layer ($\delta/U_\infty = 26\,\mu s$) is about 0.1. This clearly shows that the particles easily track the large-scale velocity fluctuations.

The PIV images from each camera were processed using TSI Insight 6.0 software which recursively refined the interrogation window from 128×128 pixels down to a size of 32×32 pixels. The physical size of the final interrogation window was $1.18\,mm$ (Magnification $\times$ window size $= 37\,\mu m/pixel \times 32$ pixels $= 1.18\,mm$). This size corresponds to a resolution of approximately 0.1δ (≈ 550 viscous wall-units), which was sufficient to capture accurately the integral length scales of the flow (to within 10%) without any effects of spatial filtering (see Spencer & Hollis 2005, also discussed in Ganapathisubramani *et al.* 2006). A 50% overlap was used to provide a vector field of size 60×60 vectors for each camera. The average streamwise pixel displacement in the upstream boundary layer was about 19 pixels. A standard 3×3 neighbourhood median filter with a tolerance of 5 pixels was utilized to remove erroneous vectors. Any missing vectors were interpolated using a 3×3 local mean technique. The number of spurious vectors was less than 2% in the dataset. The individual vector fields from all three cameras were stitched together to obtain a continuous field of view of size $\approx 9\delta \times 3\delta$ (180×60 vectors).

2.3. *Planar laser scattering (PLS)*

The flow was also visualized with high-repetition-rate planar laser scattering where the scattering medium was condensed acetone fog. The setup for PLS imaging was similar to that used for the PIV measurements, except that a single laser and camera were used. A diode-pumped Nd:YLF laser (Coherent Evolution-90, output wavelength of $527\,nm$) at a repetition rate of $10\,kHz$ was used as the light source. This laser was optimized to produce approximately $90\,W$ of power, which results in about 9 mJ per pulse at $10\,kHz$.

The fog was generated by seeding the flow with acetone droplets by using two fine-spray atomizing nozzles 6 m upstream of the stagnation chamber. The droplets evaporate before reaching the nozzle and then condense into a fine fog owing to the isentropic cooling through the nozzle. The light scattered by the acetone fog was imaged with one high-framing rate CMOS camera (Photron FASTCAM-Ultima APX) fitted with a Nikon MicroNikkor 105 mm lens with an aperture setting of f/2.8. The camera resolution was 512×256 pixels (streamwise $\times$ spanwise), and the field of
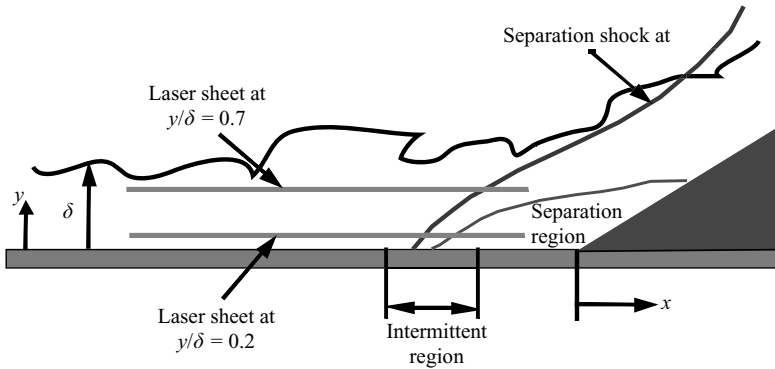
FIGURE 2. Schematic of the compression ramp interaction.

view was $76 \times 34 \, \text{mm}^2$. Further details on the PLS system can be found in Bueno *et al.* (2005). Planar laser scattering data were acquired at two wall-normal locations, $y/\delta = 0.2$ and 0.7 (the same locations as for PIV measurements).

3. Results and discussion

In all results presented in this section, x, y and z are streamwise, wall-normal and spanwise directions, respectively. The coordinates are normalized by the 99 % boundary layer thickness (δ). The origin in the streamwise direction ($x/\delta = 0$) is located at the corner of the ramp as shown in figure 2. The origin in the spanwise direction ($z/\delta = 0$) is along the centreline of the test section.

3.1. *Planar laser scattering results*

A PLS image is a representation of the intensity of the light scattered by the condensed acetone droplets in the flow. High- and low-signal intensity regions correspond to the presence and absence of acetone droplets respectively. The droplets tend to evaporate in regions with relatively high static temperature (T) and such regions exhibit low signal levels. If we assume a constant stagnation temperature (T_o) and use the energy equation ($C_p T_o = C_p T + 0.5 U^2$, where C_p is the specific heat at constant pressure, T is the local static temperature and U is the local streamwise velocity), then the regions of high static temperature are also regions of low velocity. Therefore, regions of low concentration of acetone fog tend to be associated with regions of low velocity. Similarly, regions of high concentration of acetone fog are regions of high velocity. We caution that this relationship between PLS signal and velocity is only approximate because the finite times for evaporation/condensation will obviously affect this interpretation.

Figure 3 shows a sample PLS image at a wall-normal location of $y/\delta = 0.2$. The separation region behind the shock is a region of low velocity and therefore the signal levels are low. The upstream boundary layer reveals a remarkable spanwise organization as indicated by alternating low- and high-intensity regions. This indicates the presence of spanwise strips of low- and high-momentum regions. The presence of long streamwise structures has been previously observed in similar flow visualization studies performed by Samimy *et al.* (1994) in the upper part of the boundary layer ($y/\delta = 0.49$ and 0.65). Furthermore, this signature is similar to those observed in low-Reynolds-number incompressible boundary layers by Ganapathisubramani *et al.* (2003) and Tomkins & Adrian (2003) and in a Mach 2 supersonic boundary layer by
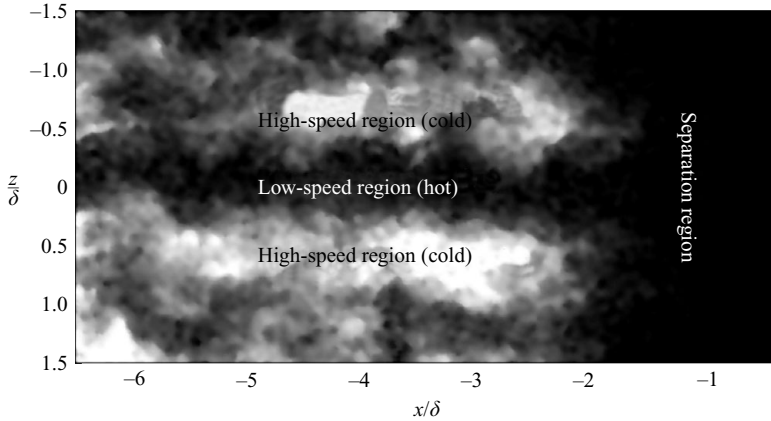
FIGURE 3. Planar laser scattering image at $y/\delta = 0.2$. The flow is from left to right. The ramp corner is at $x/\delta = 0$.

Ganapathisubramani *et al.* (2006). The instantaneous separation line (defined as the spanwise line at any given wall-normal location that defines the upstream envelope of the separated flow) seems to be farther upstream where the upstream boundary layer is slow. Conversely, the separation line is pushed downstream if the upstream boundary layer is fast. This observation is consistent with the other studies in the literature that have correlated the velocity fluctuations in the upstream boundary layer with the motion of separation shock foot (see Beresh *et al.* 2002). This feature is further discussed in §3.2, where quantitative PIV data reinforces this observation.

Figure 4 shows a time sequence of images at $y/\delta = 0.2$. The time between each image in the sequence is $100\,\mu s$, during which the flow structures travel across about 60 % of the frame. Some of the images in figure 4 clearly reveal streamwise strips of regions of high and low signal intensity. Also, the separation region seems to extend to a distance of 2δ upstream of the ramp corner. Examination of various sequences of PLS images reveal that the strips of low and high intensity are not stationary (in the spanwise direction). They appear across all possible spanwise locations and the mean of all PLS images does not show any sign of stationary structures.

Although it is possible to track turbulent structures from one frame to the next in figure 4, the displacements are too large for the motion to appear continuous as structures nominally travel a distance of about 3.5δ (60 % of the frame) between successive frames. However, Taylor's frozen turbulence hypothesis that allows conversion of time series data into spatial data can be applied to a sequence of images to deduce the streamwise extent of the coherent structures. This can be achieved by choosing an image in a sequence as the first block and shifting successive images in the streamwise direction by a distance Δx such that $\Delta x = -U_c \Delta t$, where $U_c = \overline{U}$ is the convection velocity, $\Delta t = 100\,\mu s$ is the time separation between successive images and $\overline{U}$ is the local mean streamwise velocity at this wall-normal location and is obtained from PIV measurements.

Figure 5 shows four examples of spatial data reconstructed from image sequences using Taylor's hypothesis at $y/\delta = 0.2$. All four examples reveal the presence of elongated strips of low and high momentum adjacent to each other. Figure 5(*d*) shows an elongated region of low momentum that extends across the entire image length ($\approx 40\delta$). These elongated structures meander significantly in the spanwise direction. Figure 5(*d*) shows that the 40δ-long low-speed region meanders a distance of about
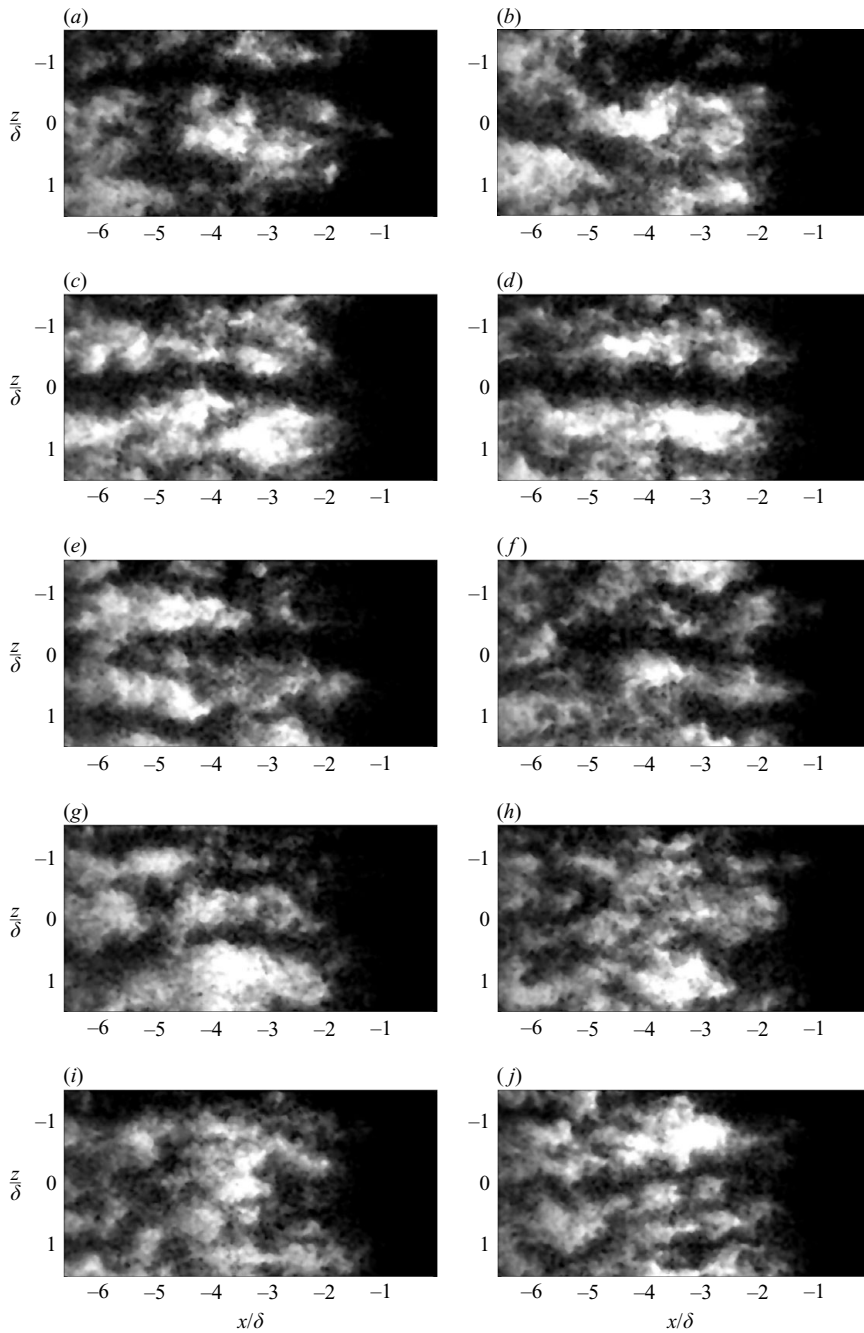
FIGURE 4. A time sequence of planar laser scattering images at $y/\delta = 0.2$.
Subsequent images are separated by 100 μs. Flow is left to right.

2δ in the spanwise direction. These elongated structures are similar to those found in
incompressible boundary layers by Hutchins *et al.* (2004), where the authors obtained
time series data at moderate Reynolds numbers ($Re_\theta \approx 2500$) using a spanwise rake
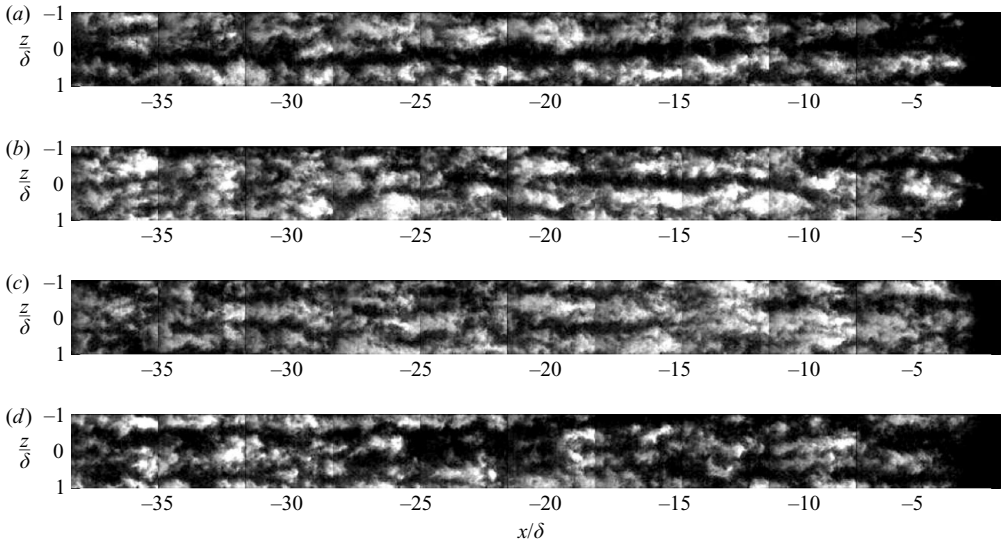of hot wires, and reconstructed the spatial extent using Taylor's hypothesis. Recently,

FIGURE 5. Examples of spatial data reconstructed using successive PLS images and Taylor's hypothesis at $y/\delta = 0.2$. Successive images are separated in time by $100\,\mu s$ and a convection velocity of $U_c = \overline{U}$ is used for reconstruction. Flow is left to right.

Hutchins & Marusic (2007) performed experiments using a rake of sonic anemometers in an atmospheric turbulent boundary layer in the salt flats in Utah (where the Reynolds number is approximately 10^6) and found signatures of similar elongated low- and high-speed regions. These elongated low- and high-speed regions appear to be a universal feature in turbulent boundary layers over a range of Reynolds numbers and Mach numbers.

Planar laser scattering image sequences can also reveal important information on the interaction dynamics, when viewed as a movie. This is particularly the case for low-frequency events that cannot be represented in sequences of images. The separation region (identified as the large region of low signal) exhibits clear unsteadiness and does not move appreciably in the $100\,\mu s$ between frames. This observation was made from viewing the movies and therefore is not apparent in the image sequences shown in figure 4. In fact, the movies are very useful for demonstrating the wide range of time scales that characterize the interaction. In particular, when the movies are played at a reasonably high framing rate (>10 f.p.s.), the upstream envelope of the separation region is seen to respond to the presence of low- and high-speed regions in the upstream boundary layer. At lower framing rates, the separation region does not seem to be correlated to the upstream boundary layer. This is evidence that the upstream boundary layer structures that drive the large-scale motion of the separation region are characterized by frequencies that are less than about 1 kHz. This conclusion is consistent with previous studies performed with cylinder interactions in a Mach 2 flow by Bueno *et al.* (2005).

Figures 6(*a*) to 6(*f*) show a sequence of 6 PLS images at the wall-normal location of $y/\delta = 0.7$. The presence of strips of uniform momentum in the upstream boundary layer is not apparent. As compared to the lower wall-normal location these PLS images seem to possess a more uniform distribution of intensity in the spanwise direction. Additionally, the images do not reveal the separation region. This could be due to the fact that the laser sheet at this wall-normal location is located above the
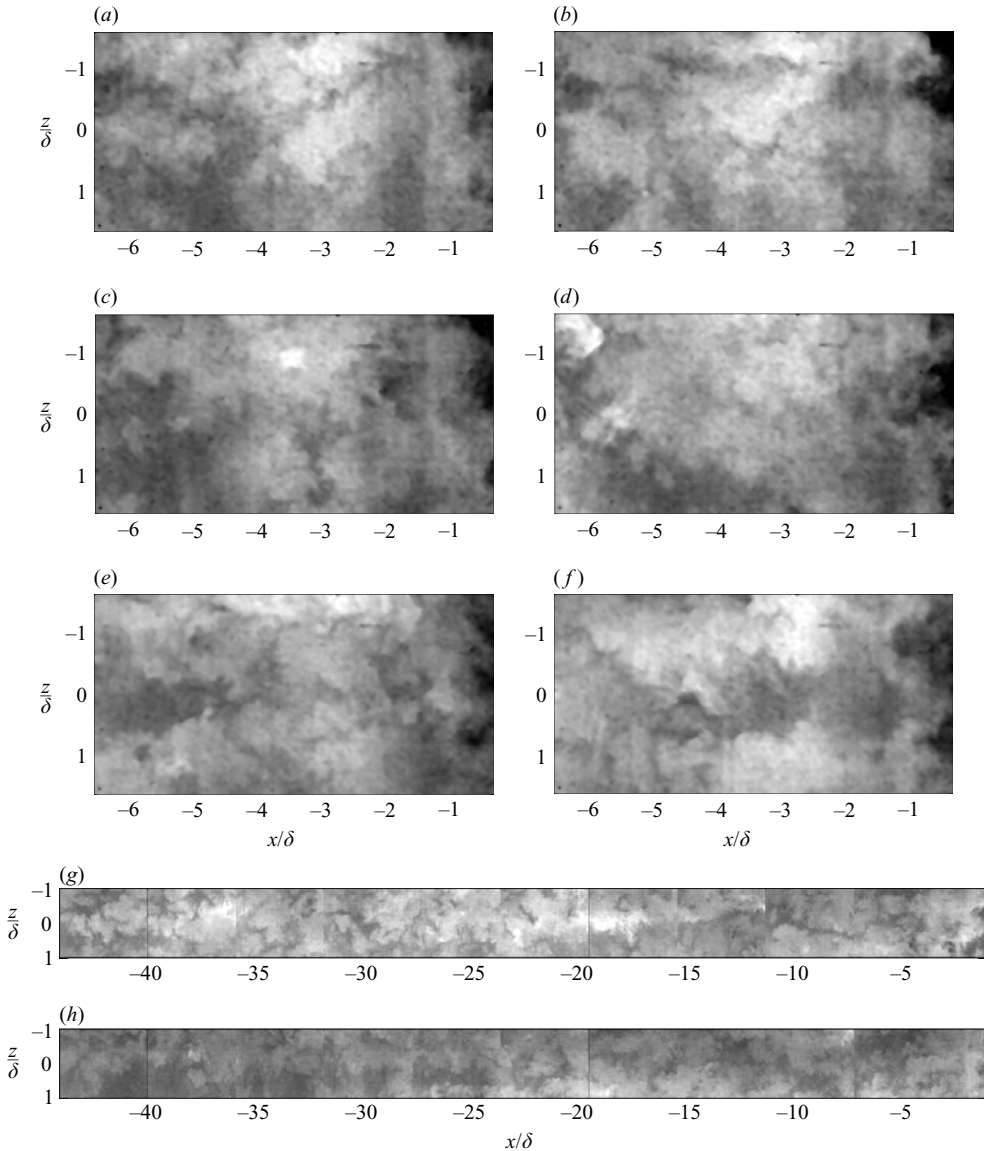
FIGURE 6. A time sequence of planar laser scattering images at $y/\delta = 0.7$. (a)–(f) Successive images separated by 100 µs. (g) and (h) Spatial extent reconstructed using successive images and Taylor's hypothesis with a convection velocity of $U_c = \overline{U}$. Flow is left to right.

separation region as illustrated in figure 2. Figures 6(g) and 6(h) shows two examples of spatial data reconstructed from image sequences using Taylor's hypothesis at $y/\delta = 0.7$. The figures do not reveal long strips of high or low intensity. The structures between successive images seem to be uncorrelated. Occasionally, a long structure spanning across two or three images is identified (as seen in the upstream end of figure 6h). Nevertheless, large-scale coherent regions are clearly not as prevalent as compared to $y/\delta = 0.2$.

The observed uniformity in intensity distribution and the absence of long coherent regions has two possible explanations. First, the velocity fluctuations at $y/\delta = 0.7$ are

much smaller than at $y/\delta = 0.2$. Therefore the variations in static temperatures are smaller and consequently so are the differences in the acetone fog concentrations. Second, studies in incompressible boundary layers indicate that elongated streamwise structures are predominantly found in the log region of the boundary layer. Therefore, it is possible that the long regions of uniform momentum just do not exist at $y/\delta = 0.7$ as the log region only extends to about $y/\delta = 0.5$ (see Ganapathisubramani *et al.* 2006).

3.2. *Wide-field particle image velocimetry results*

3.2.1. *Instantaneous results*

Figures 7 and 8 show sample PIV vector and contour plots at $y/\delta = 0.2$ and 0.7 respectively. The flow structures observed in the samples are representative of those found in many realizations. The coordinates are normalized by the boundary layer thickness (δ). The origin in the streamwise direction ($x/\delta = 0$) is located at the ramp corner as shown in figure 2. All velocity components are normalized by the free-stream velocity ($U_\infty = 510\,\mathrm{m\,s^{-1}}$). The three cameras utilized in obtaining the wide field of view are not perfectly matched in the spanwise direction. The field of view of the first camera (the camera that images the separation region) is slightly mismatched in the spanwise direction compared to the other two cameras and this mismatch can be observed in figures 7 and 8. Note that this mismatch does not affect the accuracy of the PIV measurements since the magnitude of the offset is known from the calibration procedure.

Figures 7(a) and 8(a) show the streamwise–spanwise velocity vector fields at $y/\delta = 0.2$ and 0.7 respectively. The two figures reveal the extent of the separation region at both wall-normal locations. In figure 7(a) the low velocity separated flow is labelled and is seen to extend upstream to a distance of about -2δ. However, the separation region is not obvious at $y/\delta = 0.7$ (figure 8a), which indicates that the plane of measurement (laser sheet) is above the separated flow and is probably in the shear layer above the separated flow (see schematic in figure 2).

Figures 7(b) and 7(c) show the streamwise velocity contours with two different colour scales at $y/\delta = 0.2$. Figure 7(b) has a colour scale that emphasizes the structure of the upstream boundary layer and figure 7(c) has an alternate colour scale that emphasizes the separation region. Figure 7(b) reveals the existence of strips of uniform high- and low-speed regions in the upstream boundary layer. These strips exhibit characteristic widths of approximately 0.25–0.5δ and they extend a large distance in the streamwise direction. The streamwise extent of these coherent regions is at least 7δ. Ganapathisubramani *et al.* (2006) performed similar experiments in the same facility (without the ramp) that revealed that these long regions extend beyond the full field of view (i.e. length $>8\delta$). The PLS results discussed in §3.1 suggest that these strips of uniform momentum extend to a streamwise length of more than 40δ. The strips also exhibit a spanwise gradient in U that is relatively large as the velocity changes by about $100\,\mathrm{m\,s^{-1}}$ ($0.2U_\infty$) over a distance of 0.25δ (i.e. 3 mm). It should be emphasized that these long structures are randomly distributed in space (i.e. not stationary) since they disappear when several vector fields are averaged (this can be seen in figure 9).

The influence of the upstream boundary layer on the structure of the separation region can be investigated by comparing figures 7(b) and 7(c). The spanwise separation line in figure 7(c) is undulated and conforms to the presence of high- and low-speed regions seen in figure 7(b). In this study, the instantaneous separation line is defined as the spanwise line at any given wall-normal location that defines the upstream envelope of the separated flow. The upstream extent of this envelope defines the
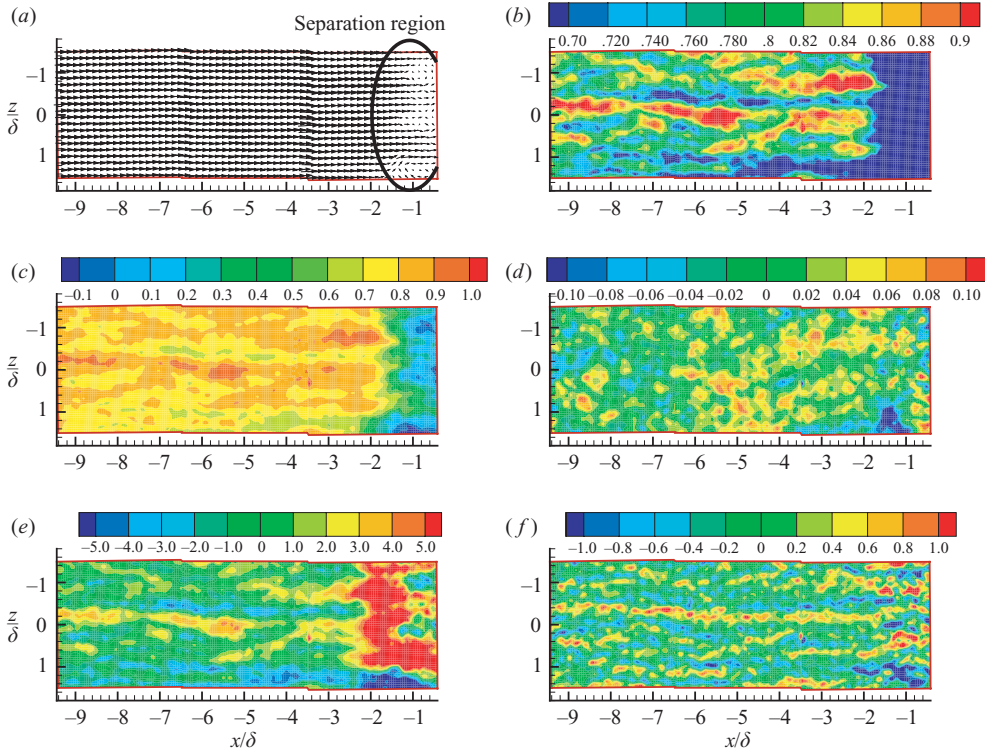
FIGURE 7. PIV results at $y/\delta = 0.2$. (*a*) Velocity vectors. The separation region is circled and marked, (*b*) U/U_∞, (*c*) U/U_∞ with a different colour scale, (*d*) W/U_∞, (*e*) u'/u_τ, (*f*) $\omega_y \delta/U_\infty$.
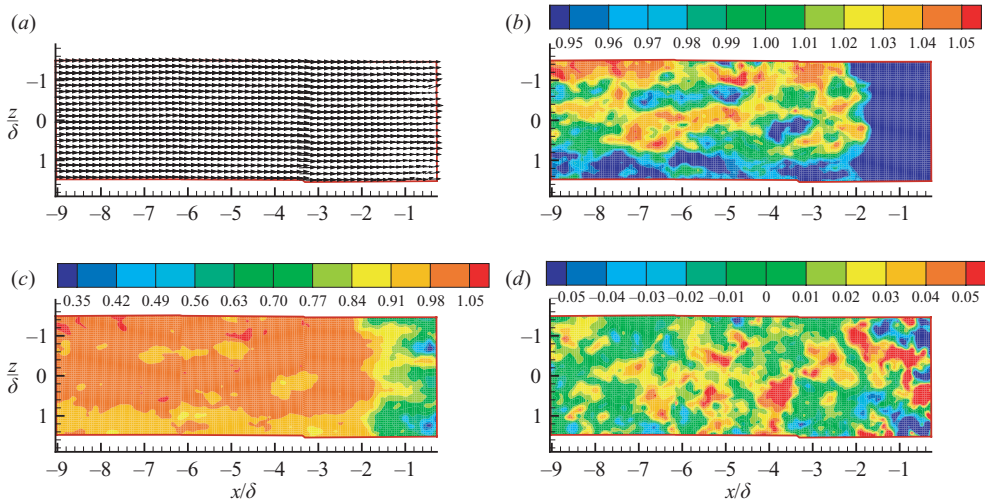

FIGURE 8. PIV results at $y/\delta = 0.7$. (*a*) Velocity vectors, (*b*) U/U_∞, (*c*) U/U_∞ with a different colour scale, (*d*) W/U_∞. Flow is from left to right.

size of the separation region. The separation region extends far upstream (at the bottom of the figures) when the upstream boundary layer has a long low-speed region. Similarly, the separation region is pushed downstream (middle of the figures), when there is a high-speed region in the upstream boundary layer. These findings are

consistent with the PLS results discussed in §3.1. It must be noted that, owing to the large range in velocities, it is necessary to view streamwise velocity fields with two different colour scales in order to deduce any relationship between the boundary layer and the separation region. Figure 7(c) together with figure 7(b) reveals a correlation between the presence of low-momentum regions in the upstream boundary layer and the existence of reverse flow in the separation region at $y/\delta = 0.2$.

Figures 8(b) and 8(c) show plots of U at $y = 0.7\delta$. Figure 8(b) has a colour scale that emphasizes the structure of the upstream boundary layer and figure 8(c) has an alternate, more global colour scale. Figure 8(b) shows that the overall structure at this location is similar to the lower wall-normal location; however, the spanwise scales are larger. Also, the range of velocities is much smaller than the range at $y/\delta = 0.2$. This is understandable since the location is practically at the edge of the boundary layer. The velocity scale of $0.95U_\infty$ to $1.05U_\infty$ was chosen to reveal the structure of the upstream boundary layer and therefore the downstream edge gives a false impression that the separation region extends upstream to about -2δ. In reality the lowest velocity in the whole field was $0.35U_\infty$, which is much higher than the lowest velocity at $y/\delta = 0.2$ (where reverse flow could be identified).

Figure 7(d) is a plot of the spanwise velocity (W) at $y/\delta = 0.2$. The velocities are in the range $\pm 50\,\mathrm{m\,s^{-1}}$ ($0.1U_\infty$). This plot reveals that spanwise velocity is far less coherent along both the streamwise and spanwise directions. The figure shows that the spatial scale of W contours is mostly short, compact and seems to appear in spanwise patches of alternating positive and negative velocity. Figure 8(d) shows a plot of W at $y/\delta = 0.7$. This plot indicates that W is more compact than U, but the W velocity signatures are longer and wider farther from the wall. This suggests that the representative length scale of the spanwise velocity fluctuations (in both streamwise and spanwise directions) increases with increasing distance from the wall.

The presence of long streamwise structures in the upstream boundary layer is in agreement with the instantaneous visualization experiments performed by Samimy *et al.* (1994) where the upper part of the boundary layer ($y/\delta = 0.49$ and 0.65) was seen to be populated with elongated longitudinal structures. The result is also consistent with the PLS results in §3.1, where regions of uniform momentum were found to extend to lengths greater than 40δ (see figure 5). However, it must also be noted that these elongated structures cannot be clearly identified in visualization experiments performed by Smith & Smits (1995). The presence of long streamwise structures is also consistent with the results of Ünalmis & Dolling (1998) who made measurements of fluctuating wall and Pitot pressures in a Mach 5 turbulent boundary layer that developed on the wind tunnel wall. They computed spanwise and streamwise cross-correlations of the pressure data, and concluded that the boundary layer exhibits streamwise vortical structures and that these structures are coherent to up to 20δ in the streamwise direction. They interpreted these elongated structures as likely resulting from Görtler-type vortices generated in the upstream nozzle. It is not known at present whether the structures observed in figures 7 and 8 are remnants of a Görtler instability, but some evidence suggests they may not be. For example, it might be expected that Görtler vortices would exhibit vorticity that is primarily streamwise, in which case the contours of W should also exhibit the presence of elongated structures with alternating positive or negative spanwise velocity.

The patterns observed in figures 7 and 8 seem to be more consistent with the velocity fields from instantaneous PIV measurements made in incompressible boundary layers by Ganapathisubramani *et al.* (2003) and Tomkins & Adrian (2003). The 'hairpin packet' model (proposed by Adrian, Meinhart & Tomkins 2000) was used in those

studies to explain the existence of instantaneous uniform momentum zones. Kim & Adrian (1999) proposed the very large-scale motion model (VLSM) which is based on the 'hairpin packet' model to explain the presence of elongated structures with lengths $>20\delta$. In this model, the elongated coherence in streamwise velocity fluctuations is caused by the presence of multiple 'hairpin packets' travelling together as a group with a common convection velocity. Ganapathisubramani *et al.* (2006) concluded that the flow signature predicted by the very large-scale motion model is similar to the observed velocity fluctuation patterns in the log region of a supersonic boundary layer (this can also be seen in figure 7*b*).

Figures 7(*e*) and 7(*f*) show the effect of the compression-ramp interaction on the turbulent structures present in the log region of the boundary layer. Figure 7(*e*) reveals streamwise velocity fluctuations u (which is computed based on the mean shown in figure 9) normalized by upstream boundary layer skin friction velocity u_τ at $y/\delta = 0.2$. The figure clearly shows that the fluctuations are amplified downstream of $x = -2.2\delta$. The fluctuations downstream of the shock (in the separation region) are at least 2–3 times higher than in the upstream boundary layer. This phenomenon of amplification of turbulent fluctuations behind a shock has been observed in both numerical and experimental studies (Andreopoulos *et al.* 2000; Agui 1998; Lee, Lele & Moin 1993; Loginov, Adams & Zheltovodov 2004). Figure 7(*f*) shows wall-normal vorticity normalized by boundary layer thickness and free-stream velocity ($\omega_y \delta / U_\infty$) at $y/\delta = 0.2$. The contours indicate amplification in vorticity behind the shock (in the separation region). The magnitude of vorticity in the separation region is 2–3 times higher than in the upstream boundary layer. This result is consistent with previous observations based on computational studies by Wu *et al.* (2005) and Zheltovodov (2006) that the separation shock acts as an amplifier of vorticity. The readers must note that the grid resolution of particle image velocimetry in the present study is not suitable for computing statistics of vorticity; however, it can be used to highlight the general point that the shock acts as an amplifier of turbulent fluctuations.

3.2.2. *Statistical results*

Figures 9(*a*) and 9(*b*) show the mean streamwise velocity at $y/\delta = 0.2$ and 0.7, respectively. The mean and r.m.s. statistics of the streamwise velocities in the upstream boundary layer are comparable to various other studies in the literature (Elena & Lacharme 1988; Smits & Dussauge 1996; Spina 1988; Hou 2003; Kistler 1959). Figures 9(*a*) and 9(*b*) show that the separation region is largely two-dimensional in the mean.

At $y/\delta = 0.7$ (figure 9*b*), the region of low streamwise velocity starting at a streamwise location of $x/\delta = -1.8$ is observed. Note that the colour scale used for this figure is different from the colour scale used in figure 9(*a*). The plane of measurement at $y/\delta = 0.7$ is above the separated flow and is located in the shear layer that is above the separation region (see figure 2). This results in a smaller deficit in the streamwise velocity in the downstream end of the image compared to the deficit observed at $y/\delta = 0.2$ (figure 9*a*).

Figures 9(*c*) and 9(*d*) show the r.m.s. fluctuations of streamwise velocity at $y/\delta = 0.2$ and 0.7. At the wall-normal location of $y/\delta = 0.2$, the r.m.s. values in the region between $x/\delta = -2$ and -1 are 4–5 times higher than the r.m.s. in the upstream boundary layer. This region of elevated r.m.s. corresponds to the intermittent region of the spanwise separation line where the unsteadiness of the separation region leads to higher fluctuations. The increased r.m.s. values can also be influenced by the amplification of turbulent fluctuations by the shock. At $y/\delta = 0.7$ (figure 9*d*), the
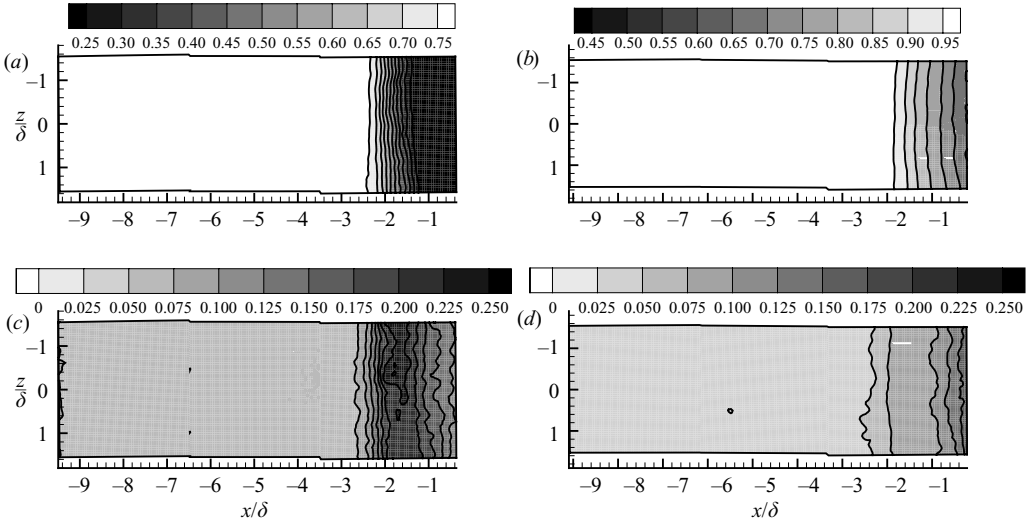
FIGURE 9. Mean and r.m.s. statistics. Mean streamwise velocity at (*a*) $y/\delta = 0.2$ and (*b*) $y/\delta = 0.7$. Root-mean-square velocity at (*c*) $y/\delta = 0.2$ and (*d*) $y/\delta = 0.7$. All mean and r.m.s. components are normalized by the free-stream velocity (U_∞).

Location (y/δ)	U_m (m s^{-1})	σ_u (m s^{-1})
0.2	397	35
0.7	502	24

TABLE 1. Mean and r.m.s. statistics of the upstream boundary layer.

r.m.s. values steadily increase downstream of $x/\delta = -1.8$ to a maximum of about 3–4 times higher than that of the upstream boundary layer. The steady increase in the r.m.s. can be attributed to the shear layer that is present above the separated flow.

To further quantify the location of the separation region, a threshold-based technique, which identifies a 'surrogate' for the true instantaneous separation line, is utilized. This technique is applied to isolate a surrogate for the separation point for all spanwise positions and the identified location is used in statistical analysis. The dataset obtained at $y/\delta = 0.2$ is used in this exercise. The data at $y/\delta = 0.7$ is not used in this analysis, since it is clear from various instantaneous velocity fields that the separation region does not extend (vertically) to this height. The measurement plane at $y/\delta = 0.7$ was located above the separated flow as shown in figure 2.

The surrogate for the separation point at a given spanwise position was defined as the streamwise point at which the instantaneous streamwise velocity is less than $U_m - 4\sigma_u$ (i.e. $U < 257 \text{ m s}^{-1}$, where U_m and σ_u are the mean and r.m.s. streamwise velocities of the upstream boundary layer). This streamwise point is identified for every spanwise location. Table 1 lists the mean and r.m.s. velocities at the two wall-normal locations. The separation point identification algorithm uses a stringent threshold to ensure that normal variations in velocity in the boundary layer are not falsely identified. In the following discussion, the 'surrogate for the separation point' will be referred to as the 'separation location'.

Threshold condition	Threshold value (m s^{-1})	U_s (m s^{-1})	σ_{u_s} (m s^{-1})
$U < U_m - 4\sigma_u$	257	92	108
$U < U_m - 6\sigma_u$	187	58	82

TABLE 2. Mean and r.m.s. statistics of the streamwise velocity in the separation region at $y/\delta = 0.2$. In this paper, the separation region is defined as the region downstream of the separation location identified using the threshold technique. The table lists the mean and r.m.s. values computed in the separation region for two different thresholds. U_s and σ_{u_s} are the mean and r.m.s. streamwise velocity components in the separation region.

The separation location directly depends on the threshold used to identify it. The identified separation location would be farther downstream if the threshold is decreased to a lower velocity. However, decreasing the threshold would decrease the number of points included in the probability distribution. Therefore, there must be a balance between the threshold used to eliminate false identification and the number of points included in the distribution. A lower velocity threshold was also used ($U < U_m - 6\sigma_u$, i.e. $U < 187\,\mathrm{m\,s^{-1}}$) to study the impact of threshold on the results.

The mean and r.m.s. statistics of the streamwise velocity were computed in the separation region and are listed in table 2. The separation region is defined as the region downstream of the separation location identified using a threshold. The table shows that both the mean and the r.m.s. values decrease with decreasing velocity threshold. A decrease in the velocity threshold pushes the separation location farther downstream where the velocity magnitude is much lower and therefore leads to a lower velocity mean. The lower r.m.s. value is consistent with the r.m.s. plot shown in figure 9(*c*) where the r.m.s. is a maximum at $x/\delta \approx -2$ and is found to decrease downstream of $x/\delta \approx -2$.

Figure 10(*a*) shows the probability distribution of the separation location at $y/\delta = 0.2$ computed using two different thresholds. The abscissa of the p.d.f. ranges from $x/\delta = -3$ to $x/\delta = 0$ in steps of 0.1δ. Note that the step size of 0.1δ is also the linear resolution of the interrogation windows used to compute the velocity vectors. For a threshold of $U < U_m - 4\sigma_u$, the most likely separation location at $y/\delta = 0.2$ is found to be at $x/\delta \approx -1.9$ and the range of the separation location varies from $x/\delta = -3$ to $x/\delta = -1$. The figure also shows the separation location possesses a normal distribution. Figure 10(*a*) also shows the p.d.f. of the separation location computed using a lower velocity threshold (i.e. $U < U_m - 6\sigma_u$). In this case, the peak in the p.d.f. is located further downstream towards the ramp corner; however, it does not alter other observed trends, but does reduce the number of points included in the p.d.f. Therefore, a threshold of $U < U_m - 4\sigma_u$ was used to identify the separation location as a balance between the number of points included in the distributions and false identification.

The distribution of the separation location in figure 10(*a*) is consistent with the shock foot location distribution deduced from wall-pressure measurements. Austin (2001) identified the shock oscillation region, in the same Mach 2 ramp interaction as used in the current study, by using wall-pressure measurements from a series of pressure transducers aligned in the streamwise direction. The author placed seven transducers underneath the intermittent region (ranging from -3.8δ to -2.2δ). Figure 10(*b*) shows a plot of the intermittency factor (γ) of the shock foot as a function of the streamwise location of those transducers (where γ is defined as the fraction of time that the shock foot is present upstream of any given transducer).
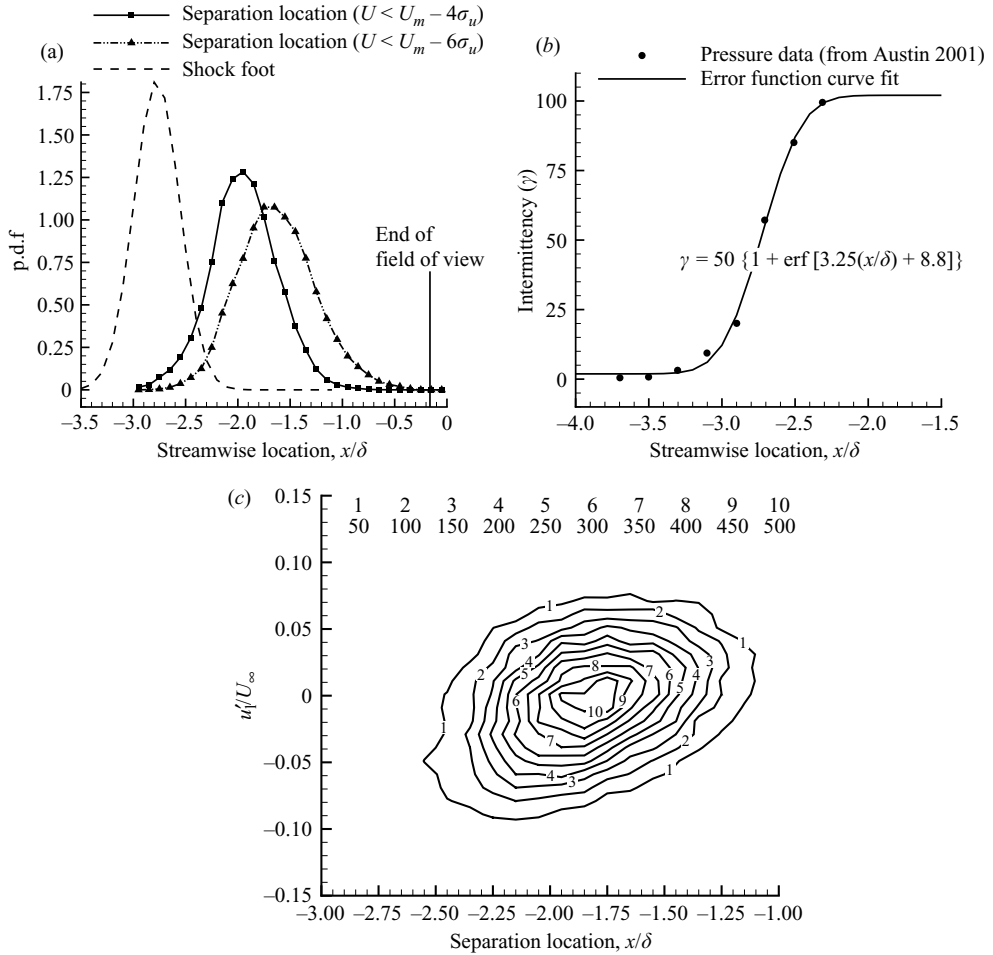
FIGURE 10. (*a*) p.d.f. of the separation location computed using two different thresholds at $y/\delta = 0.2$ and the p.d.f. of the shock foot location computed from the error function fit to intermittency factor (γ). The p.d.f. ranges from $x/\delta = -3$ to $x/\delta = 0$ in steps of 0.1δ. (*b*) Intermittency factor for the shock foot location as a function of streamwise location: data from Austin (2001). (*c*) Joint p.d.f. between the separation location and the line-averaged streamwise velocity fluctuation (u'_l) in the upstream boundary layer along the line of the separation location at $y/\delta = 0.2$. The velocity fluctuation is normalized by the free-stream velocity U_∞.

Intermittency (γ) is found to follow an error function and figure 10(*b*) also shows the error function fit to the intermittency data obtained by Austin (2001).

Figure 10(*a*) also shows the distribution of the shock foot location as a function of streamwise distance. This distribution was computed by differentiating the error function fit for γ in figure 10(*b*) with respect to x (i.e. $d\gamma/dx$, which gives a Gaussian distribution). The resulting distribution for the shock foot is seen to be similar to that of the separation location. The peak in the shock foot location p.d.f. is at -2.8δ, which is upstream of the peak in the separation point distribution. This is not surprising, considering the fact that the measurement plane is located at $y/\delta = 0.2$. The separation region would be expected to be nominally farther downstream of the shock foot at this height, as seen in figure 2.

Hou (2003) also located the shock foot with a series of pressure transducers and found that the range of motion of the shock foot was approximately 2δ ($-3.5 < x/\delta < -1.5$). Figure 10(a) shows that the range of motion of the separation point in the present study is also about 2δ ($-3 < x/\delta < -1$). Furthermore, Hou (2003) showed that the shock foot is not necessarily followed immediately downstream by separation as was suggested by Erengil & Dolling (1993). Nevertheless, this consistency in the range of motion of the shock foot and the separation region and the similarity in the shapes of the two distributions in figure 10(a) reinforces the general inference by Erengil & Dolling (1993) that the low-frequency unsteadiness of the shock foot is related to the 'breathing motion' of the separation bubble.

Joint probability density functions between the separation location and the streamwise velocity fluctuation in the upstream boundary layer were computed to investigate the correlation between the velocity fluctuations in the upstream boundary layer and the instantaneous separation location. A line-averaged streamwise velocity fluctuation along a streamwise line upstream of an identified separation location is computed for every spanwise position. This line-averaged streamwise velocity fluctuation (u_l') is defined as $U_l - U_m$, where U_l is the line-averaged streamwise velocity along a streamwise line that extends upstream from the separation location to the end of the field of view (on average, the length over which this mean is computed is about 6δ). U_m is the mean streamwise velocity of the upstream boundary layer.

Figure 10(c) shows the joint p.d.f. between the line-averaged streamwise velocity fluctuation (u_l') and the separation location at $y/\delta = 0.2$. The separation location is nominally at $x/\delta \approx -1.8$ when $u_l' \approx 0$. This suggests that this location is the neutral position for the separation region at this height. The contours are elliptical and the major axis of the ellipse is seen to be inclined. Although the elliptical nature of the contours is dependent on the scale, the inclination of the contours indicate that when u_l' is less than zero in the upstream boundary layer, the separation location is more likely to be upstream; whereas, if u_l' is greater than zero, then the separation location is more likely to be pushed downstream. The line-averaged velocity fluctuation ranges from $-0.1U_\infty$ (when the separation location is upstream) to $+0.1U_\infty$ (separation location downstream). This range in velocity fluctuations is comparable to previous studies conducted by Hou (2003) where the upstream boundary layer was found to be slower by about 30–40 m s^{-1} ($\approx 0.08U_\infty$) when the shock foot was located at its most extreme upstream position; similarly the boundary layer was faster by the same amount when the shock was located downstream.

The correlation coefficient between the two parameters (u_l' and the separation location) was computed to assess further their dependence on each other. The value of the coefficient was found to be 0.4, which also points to the existence of a relationship between the location of the separation point and the velocity fluctuation in the upstream boundary layer. It must be noted that the line-averaged velocity fluctuation (u_l') was computed along a streamwise line, whereas the long low- and high-speed regions meander in the spanwise direction. This spanwise meandering should reduce the strength of u_l' (which is computed along a straight line) and consequently decrease the value of the correlation coefficient. Also, the velocity fluctuation at a point in an elongated region of uniform momentum in the upstream boundary layer will only affect the separation region in the future, since the region convects downstream. Therefore the correlation between the separation point and the velocity fluctuation in the upstream boundary layer at any given instant would be expected to be reduced (compared to correlation between velocity fluctuation at a given instant and the separation location at an appropriate instant in the future).

Additionally, results from Beresh *et al.* (2002) and Hou (2003) (both studies perfor-med streamwise–wall-normal plane PIV measurements in the upstream boundary layer and simultaneously tracked the streamwise location of the shock foot with an array of fast-response pressure transducers) indicate that the velocity fluctuations in the upstream boundary layer are correlated to the motion of the shock foot. Both studies found that the shock foot has a tendency to move upstream when the upstream boundary layer is slower than the mean; and downstream when the upstream boundary layer is faster. Both studies concluded that the velocity fluctuation in the upstream boundary layer has a stronger correlation with the *motion* of shock foot than the *location* of the shock foot. The presence of this correlation would act to decrease the value of correlation coefficient between the separation location (which is analogous to the shock foot) and the velocity fluctuation in the upstream boundary layer.

At present, it is not feasible to perform simultaneous streamwise–spanwise plane PIV measurements and wall-pressure measurements. The pressure transducers scatter laser light and diminish the quality of PIV images. Therefore, the current study cannot confirm the correlation between the motion of the shock foot and the upstream boundary layer as found by Beresh *et al.* (2002) and Hou (2003). However, the results from the planar laser scattering measurements, the probability distributions and the instantaneous PIV fields presented in this study in conjunction with those previous studies, show that the long low- and high-speed regions in the upstream boundary layer have a clear effect on the unsteadiness of the separation region.

The relationship between the upstream boundary layer and the separation location can be further examined by computing averages of the velocity field conditioned on the separation location. Two separation locations were considered: one where the separation location was far upstream and one where it was far downstream. Figure 11(a) shows an average velocity fluctuation field conditioned on the separation location present upstream of -2.2δ (i.e. $x_{sep}/\delta < -2.2$). The conditional point is located along $z/\delta = 0$ and a total spanwise width of $3.6\,\delta$ is shown in the figure. A constant streamwise velocity equal to the mean streamwise velocity in the upstream boundary layer (U_m) is subtracted from the conditionally averaged velocity field to emphasize the fluctuations in the upstream boundary layer. The contours/shading is blocked off in regions where the velocity is less than the threshold used to identify the separation location (the solid white region in the downstream end of the image represents the separated flow). Figure 11(a) clearly reveals the presence of an elongated low-speed region, upstream of the separation location. The upstream envelope of the separated flow is undulated in accordance with the presence of a low-speed region. The average streamwise velocity fluctuation in the upstream low-speed region is approximately equal to $-0.025U_\infty$. Figure 11(b) shows an average velocity field conditioned on the separation location being present downstream of -1.4δ (i.e. $x_{sep}/\delta > -1.4\delta$). This plot exhibits a long high-speed region located upstream of the separation location and the envelope of the separated flow conforms to the existence of the high-speed region in the upstream boundary layer. The mean streamwise velocity fluctuation in the upstream high-speed region is about $0.025U_\infty$. The difference in the magnitude between the low-speed and the high-speed regions in the upstream boundary layer ($\approx 0.05U_\infty$) is consistent with the results from joint p.d.f. analysis and is comparable to the range depicted in the study performed by Hou (2003).

It must be noted that the average velocity contours in figures 11(a) and 11(b) are not well converged owing to lack of sufficient data. Moreover, the spanwise meandering of elongated low- and high-speed regions and the range of scales over which these
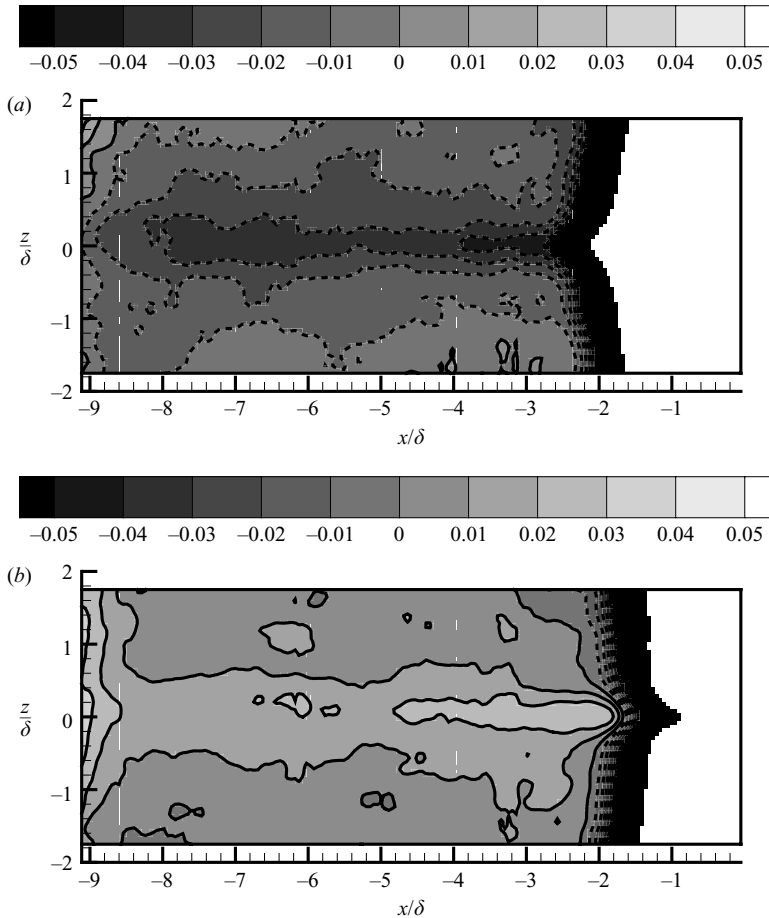
FIGURE 11. Conditionally averaged streamwise velocity fluctuation fields. The mean streamwise velocity in the upstream boundary layer (U_m) is subtracted from the conditionally averaged velocity field to obtain the fluctuations. (*a*) The velocity fluctuation field is conditioned on the location of separation, which is upstream of -2.2δ. (*b*) The velocity fluctuation field is conditioned on the separation location, which is downstream of -1.4δ. Contour lines are also shown for the sake of clarity. The negative contours are shown as dashed lines. The fluctuations are normalized by U_∞.

structures are present in the boundary layer act to reduce the magnitude of the velocity fluctuations in the conditional averages. Regardless, figures 11(*a*) and 11(*b*) provide qualitative information that reveals the impact of the upstream boundary layer on the separation location and reinforces the presence of a definite relationship between the elongated regions of uniform momentum and the separation location (the surrogate for the separation point).

4. Summary and discussion

The instantaneous results presented in the previous section indicate the presence of elongated regions of uniform momentum in the upstream supersonic boundary layer. These elongated regions seem to play a significant role in the unsteadiness of the separated flow in shock boundary layer interactions. The upstream envelope of

the separated flow is found to be undulated and conforms to the presence of high- and low-speed regions in the upstream boundary layer. The separation location (as identified by a threshold technique) is found to be farther downstream in the presence of a high-speed region in the upstream boundary layer. Conversely, the separation location is positioned upstream in the presence of a low-speed region.

A representative frequency of unsteadiness can be computed based on the streamwise length of these coherent regions and a convection velocity. The PLS results in §3.1 indicate that these elongated regions extend to lengths greater than 40δ. For example, the frequency of unsteadiness based on a 40δ long streamwise structure is $U_\infty/40\delta \approx 1000\,\mathrm{Hz}$. This representative frequency is an order of magnitude lower than the characteristic boundary layer frequency of $U_\infty/\delta \approx 40\,\mathrm{kHz}$ and is entirely consistent with the frequency of unsteadiness of the separation region/shock foot observed in previous experimental studies (see Erengil & Dolling 1993; Beresh *et al.* 2002; Hou 2003; Bueno *et al.* 2005). It must also be noted that the wavelength corresponding to a 40δ-long region of uniform momentum would in fact be 80δ (if we consider a 40δ-long low-speed region followed by a high-speed region with the same length). Since frequency is based on a wavelength, the actual frequency of unsteadiness would be half the value reported above, i.e. $U_\infty/80\delta \approx 500\,\mathrm{Hz}$. Therefore, the presence of elongated low- and high-speed regions over a range of streamwise length scales would account for the range of frequencies for the unsteadiness of the shock foot/separation region observed by various studies in the literature.

Although the presence of elongated regions of uniform momentum could be a mechanism responsible for the low-frequency unsteadiness of the shock foot, alternate explanations for the low-frequency unsteadiness are also possible and have been presented in the literature. For example, as discussed earlier in §1, Plotkin (1975) proposed a mathematical model for the low-frequency unsteadiness. Plotkin's model was based on a linear restoring mechanism for the shock foot where the constant that defines the restoring mechanism was determined based on the premise that the time scale of velocity fluctuations (τ_u) is considerably smaller than the time scale of shock unsteadiness (τ_s). However, results presented in this study indicate that the boundary layer not only consists of high-frequency small-scale structures but also low-frequency, large-scale structures. Recently, Poggie & Smits (2005) presented experimental evidence based on wall-pressure data that support Plotkin's model for the shock foot unsteadiness, but the authors found that the model has a relatively poorer fit in regions where the flow possesses a considerable low-frequency energy content (in which case the assumption $\tau_u \ll \tau_s$ may not be appropriate). However, a physical model that includes the presence of elongated regions of uniform momentum can co-exist with the mathematical model proposed by Plotkin (1975), although the constant that defines the restoring mechanism has to be re-evaluated to account for the presence of large-scale structures.

The three-dimensional nature of the separation bubble and the possible acoustic resonance between the separated flow and the shock foot have also been considered as possible explanations for the low-frequency unsteadiness of the shock foot/separated flow. Recently, Dussauge, Dupont & Debieve (2006) performed experimental in-vestigations (pressure measurements and PIV) in a reflected shock/boundary layer interaction and concluded that the three-dimensional structure of the separation bubble may be responsible for the low-frequency unsteadiness. Pirozzoli & Grasso (2006) performed numerical studies (DNS) of a reflected shock wave/boundary layer interaction and proposed that the large-scale low-frequency unsteadiness is due to a resonance mechanism that establishes in the interaction region. They claimed that

the mechanism is similar to those responsible for the generation of tones in cavity flows and screeching jets. The authors developed a simplified model for the acoustic resonance that is capable of predicting the characteristic frequencies of the tones.

A physical explanation for the unsteadiness of the shock foot/separation region based on the results in the previous sections (i.e. the presence of elongated regions of uniform momentum) is as follows. The instantaneous separation point either moves upstream, or is located at an upstream location in the presence of a low-speed region in the upstream boundary layer. Similarly, the presence of a high-speed region in the upstream boundary layer results in downstream motion or a downstream location of the separation point. The spanwise separation line is undulated conforming to the presence of these high and low-speed regions. The frequency at which the separation point moves upstream/downstream or is located at an upstream/downstream position depends on the streamwise length of the low/high momentum region and the convection velocity of the coherent structure. The minor velocity fluctuations within an elongated streamwise structure and other relatively small-scale vortical structures within the boundary layer could cause the small-scale jitter that is found to be superimposed on the predominant low-frequency unsteadiness.

Dussauge (2001) listed three possible influences that could contribute to the unsteadiness observed in shock/boundary layer interactions: first, the turbulence structure of the incoming boundary layer, second, the independent characteristic time and length scales of the separated flow, and finally the unsteady upstream and downstream conditions that could make the shock fluctuate according to its own frequency response. The author also stated that it would be necessary to understand all three influences and investigate the possibility of potentially coupling them. In the current study, the contribution of the upstream boundary layer was explored in detail. The presence of the elongated regions of uniform momentum was found to be responsible for the undulation present in the upstream envelope of the separated flow. This finding does not preclude the presence of an independent characteristic time/length scale within the separated flow or a resonance-type mechanism between the separated flow and the shock foot. However, based on the results obtained in this study, it is likely that the time/length scales of the separated flow, and/or the resonance, are coupled with the length/time scales present in the upstream boundary layer. Further investigations are necessary to isolate these coupled characteristics.

5. Conclusions

Wide-field particle image velocimetry and $10\,\text{kHz}$ planar laser scattering measurements were performed in streamwise–spanwise planes of a shock wave/turbulent boundary layer interaction generated by a $20°$ ramp in a Mach 2 flow. PLS imaging of the upstream boundary layer revealed elongated regions of low- and high-speed fluid that extend to streamwise lengths greater than 40δ (length computed based on Taylor's hypothesis). In addition, the separation region was found to respond to these low- and high-speed regions.

The wide-field PIV measurements of the interaction were made using three cameras to capture a large part of the upstream boundary layer and a considerable portion of the separation region. Measurements were made at two wall-normal locations ($y/\delta = 0.2$ and 0.7). Instantaneous velocity fields show the presence of long regions of uniform momentum (both high- and low-momentum) in the upstream boundary layer. The presence of elongated low- and high-speed regions is remarkably similar to the signature observed in incompressible boundary layers. The uniform momentum

regions seem consistent with the 'very large-scale motions' model proposed by Kim & Adrian (1999) to explain the presence of similar structures in incompressible boundary layers.

The instantaneous spanwise separation line of the shock-induced separation region is seen to be undulated, conforming to the presence of high- and low-speed regions in the upstream boundary layer. Statistical analysis utilizing joint p.d.f.s, conditional averages and observations of various instantaneous velocity fields indicate that the location of separation is pushed downstream if the upstream boundary layer is faster. Conversely, the separation location moves upstream if the boundary layer is slower.

Instantaneous PLS and PIV fields and the statistical results computed based on PIV fields indicate that the presence of elongated low- and high-speed regions in the boundary layer is due to a turbulent mechanism that can account for the low-frequency unsteadiness of the shock-induced separation region found in various shock/boundary layer interactions.

REFERENCES

ADRIAN, R. J., MEINHART, C. D. & TOMKINS, C. D. 2000 Vortex organization in the outer region of the turbulent boundary layer. *J. Fluid Mech.* **422**, 1–53.

AGUI, J. H. 1998 Shock wave interactions with turbulence and vortices. PhD thesis, City University, New York.

DEL ALAMO, J. C., JIMENEZ, J., ZANDONADE, P. & MOSER, R. D. 2004 Scaling of the energy spectra of turbulent channels. *J. Fluid Mech.* **500**, 135–144.

ANDREOPOULOS, J. & MUCK, K. C. 1987 Some new aspects of the shock-wave boundary layer interaction. *J. Fluid Mech.* **180**, 405–428.

ANDREOPOULOS, Y., AGUI, J. H. & BRIASSULIS, G. 2000 Shock wave–turbulence interactions. *Annu. Rev. Fluid Mech.* **32**, 309–345.

AUSTIN, R. G. 2001 Effect of upstream pulsed mass injection on a Mach 2 shockwave–turbulent boundary layer interaction. Master's thesis. Department of Aerospace Engineering and Engineering Mechanics, The University of Texas at Austin, Texas, USA.

BERESH, S. J., CLEMENS, N. T. & DOLLING, D. S. 2002 Relationship between upstream turbulent boundary-layer velocity fluctuations and separation shock unsteadiness. *AIAA J.* **40**, 2412–2422.

BRUSNIAK, L. & DOLLING, D. S. 1994 Physics of unsteady blunt-fin-induced shock wave-turbulent boundary layer interactions. *J. Fluid Mech.* **273**, 375–409.

BUENO, P. C., GANAPATHISUBRAMANI, B., CLEMENS, N. T. & DOLLING, D. S. 2005 Cinematographic planar imaging of a Mach 2 shock wave turbulent boundary layer interaction. *AIAA Paper* 2005-0441.

DOLLING, D. S. 1993 Fluctuating loads in shock wave-turbulent boundary layer: Tutorial and Update. *AIAA Paper* 1993-0284.

DOLLING, D. S. 1998 High-speed turbulent separated flows: Consistency of mathematical models and flow physics. *AIAA J.* **36**, 725–732.

DOLLING, D. S. 2001 Fifty years of shock-wave/boundary-layer interaction research: What next? *AIAA J.* **39**, 1517–1531.

DOLLING, D. S. & BRUSNIAK, L. 1989 Separation shock motion in fin, cylinder and compression ramp induced turbulent interactions. *AIAA J.* **27**, 734–742.

DUSSAUGE, J. P. 2001 Compressible turbulence and energetic scales: What is known from experiments in supersonic flows? *Flow, Turbulence Combust.* **66**, 373–391.

Dussauge, J. P., Dupont, P. & Debieve, J. F. 2006 Unsteadiness in shock wave boundary layer interactions with separation. *Aero. Sci. Technol.* **10**, 85-91.

Elena, M. & Lacharme, J. P. 1988 Experimental study of a supersonic turbulent boundary layer using a laser doppler anemometer. *J. Theoret. Appl. Mech.* **7**, 175–190.

Erengil, M. E. & Dolling, D. S. 1993 Physical causes of separation shock unsteadiness in shock wave/turbulent boundary layer interactions. *AIAA Paper* 1993-3134.

Ganapathisubramani, B., Clemens, N. T. & Dolling, D. S. 2006 Large scale motions in a supersonic turbulent boundary layer. *J. Fluid Mech.* **556**, 271–282.

Ganapathisubramani, B., Longmire, E. K. & Marusic, I. 2003 Characteristics of vortex packets in turbulent boundary layers. *J. Fluid Mech.* **478**, 35–46.

Hou, Y. X. 2003 Particle image velocimetry study of shock induced turbulent boundary layer separation. PhD thesis, Department of Aerospace Engineering and Engineering Mechanics, The University of Texas at Austin, Texas, USA.

Hou, Y. X., Clemens, N. T. & Dolling, D. S. 2003 Wide-field PIV study of shock-induced turbulent boundary layer separation. *AIAA Paper* 2003-0441.

Hutchins, N., Ganapathisubramani, B. & Marusic, I. 2004 Dominant spanwise Fourier modes and existence of very large scale coherence in turbulent boundary layers. In 15th *Australasian Fluid Mechanics Conference, December 13–17, Sydney, Australia.*

Hutchins, N. & Marusic, I. 2007 Evidence of very long meandering features in the logarithmic region of turbulent boundary layers. *J. Fluid Mech.* **579**, 1–28.

Kim, K. C. & Adrian, R. J. 1999 Very large-scale motion in the outer layer. *Phys. Fluids* **11**, 417–422.

Kistler, A. L. 1959 Fluctuation measurements in supersonic turbulent boundary layer. *Phys. Fluids* **2**, 290–296.

Lee, L., Lele, S. K. & Moin, P. 1993 Direct numerical simulation of isotropic turbulence interacting with a weak shock wave. *J. Fluid Mech.* **251**, 533–562.

Loginov, M., Adams, N. & Zheltovodov, A. 2004 Large-eddy simulation of shock-wave/turbulent boundary layer interaction. In 21st *ICTAM, August 15–21, Warsaw, Poland*.

McClure, W. B. 1992 An experimental study of the driving mechanism and control of the unsteady shock induced turbulent separation in a Mach 5 compression corner flow. PhD thesis, Department of Aerospace Engineering and Engineering Mechanics, The University of Texas at Austin, Texas, USA.

Owen, F. K. & Horstmann, C. C. 1972 On the structure of hypersonic turbulent boundary layers. *J. Fluid Mech.* **53**, 611–636.

Pirozzoli, S. & Grasso, F. 2006 Direct numerical simulation of impinging shock wave/turbulent boundary layer interaction at M = 2.25. *Phys. Fluids* **18**, 065113.

Plotkin, K. J. 1975 Shock wave oscillation driven by turbulent boundary layer fluctuations. *AIAA J.* **13**, 1036–1040.

Poggie, J. & Smits, A. J. 2005 Experimental evidence for Plotkin model of shock unsteadiness in separated flow. *Phys. Fluids* **17**, 018107.

Samimy, M., Arnette, S. A. & Elliot, G. S. 1994 Streamwise structures in a supersonic turbulent boundary layer. *Phys. Fluids* **6**, 1081–1083.

Samimy, M. & Lele, S. K. 1991 Motion of particles with inertia in a compressible free shear layer. *Phys. Fluids* A **3**, 1915–1923.

Smith, M. W. & Smits, A. J. 1995 Visualization of the structure of supersonic turbulent boundary layers. *Exp. Fluids* **18**, 288–302.

Smits, A. J. & Dussauge, J. P. 1996 *Turbulent Shear Layers in Supersonic Flow*. American Institute of Physics Press.

Smits, A. J., Spina, E. F., Alving, A. E., Smith, R. W., Fernando, E. M. & Donovan, J. F. 1989 A comparison of the turbulence structure of subsonic and supersonic boundary layers. *Phys. Fluids* A **1**, 1865–1875.

Spencer, A. & Hollis, D. 2005 Correcting for sub-grid filtering effects in particle image velocimetry data. *Meas. Sci. Technol.* **40**, 2323–2335.

Spina, E. F. 1988 Organized structures in a supersonic turbulent boundary layer. PhD thesis, Department of Mechanical and Aerospace Engineering, Princeton University, NJ, USA.

Tomkins, C. D. & Adrian, R. J. 2003 Spanwise structure and scale growth in turbulent boundary layers. *J. Fluid Mech.* **490**, 37–74.

ÜNALMIS, O. H. & DOLLING, D. S. 1994 Decay of wall pressure field and structure of a Mach 5 adiabatic turbulent boundary layer. *AIAA Paper* 94-2363.

ÜNALMIS, O. H. & DOLLING, D. S. 1998 Experimental study of causes of unsteadiness of shock induced turbulent separation. *AIAA J.* **36**, 371–378.

WU, M., BOOKE, P., MARTIN, M. P. & SMITS, A. J. 2005 Analysis of shockwave/turbulent boundary layer interactions using DNS and experimental data. *AIAA Paper* 2005-0310.

ZHELTOVODOV, A. 2006 Some advances in research of shock wave turbulent boundary layer interactions. *AIAA Paper* 2006-0496.